Research Article Vol. 27, No. 20 | 30 Sep 2019 | OPTICS EXPRESS 28114

Optics EXPRESS

Gauge-field description of Sagnac frequency shift and mode hybridization in a rotating cavity

HONGKANG SHI,[1] ZHONGFEI XIONG,[1] WEIJIN CHEN,[1] JING XU,[1,2]
SHUBO WANG,[3,4] AND YUNTIAN CHEN,[1,2,*]

[1] *School of Optical and Electronic Information, Huazhong University of Science and Technology, Wuhan, China*
[2] *Wuhan National Laboratory for Optoelectronics, Huazhong University of Science and Technology, Wuhan, China*
[3] *Department of Physics, City University of Hong Kong, Hong Kong, China*
[4] *shubwang@cityu.edu.hk*
[*] *yuntian@hust.edu.cn*

Abstract: Active optical systems can give rise to intriguing phenomena and applications that are not available in conventional passive systems. Structural rotation has been widely employed to achieve non-reciprocity or time-reversal symmetry breaking. Here, we examine the quasi-normal modes and scattering properties of a dielectric disk under rotation. In addition to the familiar phenomenon of Sagnac frequency shift, we observe the the hybridization of the clockwise (CW) and counter-clockwise CCW) chiral modes of the cavity controlled by the rotation. The rotation tends to suppress one chiral mode while amplifying the other, and it leads to the variation of the far field. The phenomenon can be understood as the result of a synthetic gauge field induced by the rotation of the cavity. We explicitly derived this gauge field and the resulting Sagnac frequency shift. The analytical results are corroborated by finite element simulations. Our results can be applied in the measurement of rotating devices by probing the far field.

1. Introduction

The rotating cavity is a rich subject with far-reaching implications and has many applications such as optical gyroscopes [1–3], as evidenced by the long record of literature in the past four decades. The rotation induced effects [4–6], such as Sagnac frequency splitting and the modified far-field pattern, can be interpreted in various ways by the stationary observer (inertial frame) and the moving observer (reference frame rotating with the cavity). Coincidentally, it is found that the first order approximation [7] in either inertial frame or rotating frame yields consistent results on the Sagnac frequency shift by using the proper non-relativistic constitutive relation for the moving medium. Interestingly, Cook and co-workers compare the time-independent Schröndinger equation with the wave-equation for the electric field in moving medium up to the first order [8], and concluded that the velocity of the moving medium $\boldsymbol{v}$ and the vorticity $\nabla \times \boldsymbol{v}$ play the roles of the vector potential and the effective magnetic field that bend light, analogous to electrons travelling in magnetic field. The similar concept as well as the first-order treatment are also used to examine the Aharonov-Bohm effect of light associated with a rotating rod immersed in a viscous fluid [9]. Considering the recent development of topological photonics, it is theoretically appealing to have a gauge field description [10–14]of the optical properties of rotating cavities beyond the first order approximation.

In this paper, with Minkowski's postulation of the modified constitutive relation of moving medium [15], we revisit the rotating two-dimensional(2D) microdisk cavity hosted in vacuum and develop a physically transparent yet rigorous description for the Sagnac frequency splitting and modal hybridization of the cavity by constructing the effective gauge field induced by rotation. In particular, we consider finite quality(Q)-factor cavity modes supported by high refractive

#369908 https://doi.org/10.1364/OE.27.028114
Journal © 2019 Received 14 Jun 2019; revised 14 Aug 2019; accepted 16 Aug 2019; published 19 Sep 2019

index dielectric disk. The rotating cavity can be equivalently treated as stationary cavity with bianisotropic response, which can be further solved by analytical or numerical approaches. From the first principle of Maxwell's equations, we analytically derive the rotation-induced gauge field, the effective magnetic field, and the Sagnac frequency splitting $\Delta\omega$, which are further benchmarked against full-wave finite-element simulations. At low rotation speed, as $\Delta\omega$ is small, the spectra of the CW and CCW resonances overlap, leading to rotation-induced evolution of far-field emission patterns as explained qualitatively by Ge et al [16]. The modal hybridization due to the spectral overlapping between the CW and CCW mode is semi-analytically described by the coherent superposition of the two quasi-normal modes in this paper.

The paper is organized as follows. In Section 2, we give the detailed derivations of rotation-induced gauge field and effective magnetic field as well as frequency splitting $\Delta\omega$. The simulation results and discussions are provided in Section 3. Finally, the paper is concluded in Section 4.

2. Fundamentals of rotation-induced gauge field

2.1. Synthetic gauge field and effective magnetic field in a rotating cavity

Figure 1(a) shows the view of a 2D circular dielectric disk(invariant along z direction) rotating around the center with angular velocity Ω, where (r, θ) are, respectively, the radial and azimuthal coordinates, and $\hat{\boldsymbol{e}}_r$ and $\hat{\boldsymbol{e}}_\theta$ are the corresponding unit vectors. The linear velocity of the rotating disk is $\boldsymbol{v} = \Omega r \hat{\boldsymbol{e}}_\theta$ at a radius r. The modified constitutive relation [15] of the moving medium in the stationary frame is given by,

$$\begin{aligned} \boldsymbol{D} + \boldsymbol{v} \times \boldsymbol{H}/c^2 &= \boldsymbol{\varepsilon}\left(\boldsymbol{E} + \boldsymbol{v} \times \boldsymbol{B}\right), \\ \boldsymbol{B} + \boldsymbol{E} \times \boldsymbol{v}/c^2 &= \boldsymbol{\mu}\left(\boldsymbol{H} + \boldsymbol{D} \times \boldsymbol{v}\right), \end{aligned} \tag{1}$$

where $\boldsymbol{E}$, $\boldsymbol{D}$, $\boldsymbol{B}$, and $\boldsymbol{H}$ are electromagnetic fields, c is the speed of light in vacuum. It is worth noting that Eq. (1) only applies to rotating objects with axial symmetry whose shapes remain unchanged compared to that in the rest frame [17]. For deformed cavities without axial symmetry, the equations will become much more complicated. Equation (1) amounts to introducing bianisotropic response to the rotating disk, and the general form of the effective constitutive relation is given by $\begin{pmatrix} \boldsymbol{D} \\ \boldsymbol{B} \end{pmatrix} = \begin{pmatrix} \bar{\boldsymbol{\varepsilon}} & \bar{\chi}_{eh} \\ \bar{\chi}_{he} & \bar{\boldsymbol{\mu}} \end{pmatrix} \begin{pmatrix} \boldsymbol{E} \\ \boldsymbol{H} \end{pmatrix}$, where $\bar{\boldsymbol{\varepsilon}} = \varepsilon_0 \bar{\boldsymbol{\varepsilon}}_r, \bar{\boldsymbol{\mu}} = \mu_0 \bar{\boldsymbol{\mu}}_r, \bar{\chi}_{eh} = \sqrt{\varepsilon_0 \mu_0} \bar{\chi}^r_{eh}$ and $\bar{\chi}_{he} = \sqrt{\varepsilon_0 \mu_0} \bar{\chi}^r_{he}$. Notably, all the elements of the material tensor explicitly depend on rotation speed Ω. In contrast to reciprocal medium which have $\bar{\boldsymbol{\varepsilon}} = \bar{\boldsymbol{\varepsilon}}^T, \bar{\boldsymbol{\mu}} = \bar{\boldsymbol{\mu}}^T$, and $\bar{\chi}_{eh} = -\bar{\chi}^T_{he}$, the rotating disk does not obey reciprocity, and the bianisotropic tensor elements satisfy $\bar{\boldsymbol{\varepsilon}} = \bar{\boldsymbol{\varepsilon}}^T, \bar{\boldsymbol{\mu}} = \bar{\boldsymbol{\mu}}^T, \bar{\chi}_{eh} = \bar{\chi}^T_{he}$. The rotation introduces non-reciprocity to the equivalent electromagnetic medium, therefore, it can be employed to realize the optical isolation [18, 19].

The source-free Maxwell's equations with time harmonic dependence $e^{-i\omega t}$ are given by $\left(\boldsymbol{\nabla} \times -ik_0 \bar{\chi}^r_{he}\right) \boldsymbol{e} = ik_0 \bar{\boldsymbol{\mu}}_r \boldsymbol{h}$ and $\left(\boldsymbol{\nabla} \times +ik_0 \bar{\chi}^r_{eh}\right) \boldsymbol{h} = -ik_0 \bar{\boldsymbol{\varepsilon}}_r \boldsymbol{e}$, where $k_0 = \omega\sqrt{\varepsilon_0 \mu_0}$, ω is the angular frequency, $\boldsymbol{e} = \boldsymbol{E}, \boldsymbol{h} = Z_0 \boldsymbol{H}$ are the normalized electromagnetic field, and Z_0 is the vacuum impedance. Considering TE modes where the electric field only has e_z component in a rotating disk, see Fig. 1(a), one arrives at the Helmholtz equation by eliminating the magnetic field $\boldsymbol{h}$ as follows,

$$\left(\frac{1}{r}\frac{\partial}{\partial\theta} + ik_0 A_\theta\right)^2 e_z + \frac{\mu_{rr}}{\mu_{\theta\theta}}\frac{1}{r}\frac{\partial}{\partial r}\left(r\frac{\partial}{\partial r}e_z\right) + k_0^2 \varepsilon_{zz}\mu_{rr} e_z = 0, \tag{2}$$

where $A_\theta = -\frac{cr\Omega(\varepsilon_r\mu_r - 1)}{c^2 - \varepsilon_r\mu_r r^2\Omega^2}$, $\mu_{rr} = \frac{\mu_r\left(c^2 - r^2\Omega^2\right)}{c^2 - \varepsilon_r\mu_r r^2\Omega^2}$, $\mu_{\theta\theta} = \mu_r$, and $\varepsilon_{zz} = \frac{\varepsilon_r\left(c^2 - r^2\Omega^2\right)}{c^2 - \varepsilon_r\mu_r r^2\Omega^2}$. Importantly, Eq. (2) gives the explicit expression of the gauge field (i.e. vector potential) in the azimuthal direction: $\boldsymbol{A} = A_\theta \hat{\boldsymbol{e}}_\theta$, which accounts for the rotation-induced effects. The effective magnetic field $\mathcal{B}$ along z axis can be obtained from the vector potential as

$$\mathcal{B} = \nabla \times \boldsymbol{A} = \frac{2\Omega\left(\varepsilon_r \mu_r - 1\right)}{c\left(1 - \varepsilon_r \mu_r r^2 \Omega^2 / c^2\right)^2} \hat{\boldsymbol{e}}_z = B_z \hat{\boldsymbol{e}}_z, \tag{3}$$

where $\hat{\boldsymbol{e}}_z$ is the unit vector in z direction.

2.2. Sagnac frequency splitting

A circular disk of radius R has a pair of CW and CCW modes with the mode electric field $e_z = E_z(r)\, e^{\pm i k_\theta r \theta}$, where $k_\theta = m/r$, the azimuthal quantum number m is a conserved quantity. Substituting it into Eq. (2), one obtains the frequency splitting between CW and CCW modes as

$$\Delta\omega = \frac{2 k_\theta A_\theta c}{\varepsilon_{zz} \mu_{rr} - {A_\theta}^2}. \tag{4}$$

In the limit of $R\Omega \ll c$, all high-order terms about Ω in Eq. (4) can be omitted, so $\varepsilon_{zz}\mu_{zz} - A_\theta^2 \approx \varepsilon_r \mu_r$, the vector potential is $A_\theta \approx \tilde{A}_\theta = \frac{R\Omega(\varepsilon_r \mu_r - 1)}{c}$, and effective magnetic field is $B_z \approx \tilde{B}_z = \frac{\Omega(\varepsilon_r \mu_r - 1)}{c}$. We then get

$$\Delta\omega = \frac{2 k_\theta \tilde{A}_\theta c}{\varepsilon_r \mu_r} = \frac{2m \tilde{B}_z c}{\varepsilon_r \mu_r} = \frac{2m(\varepsilon_r \mu_r - 1)\Omega}{\varepsilon_r \mu_r}, \tag{5}$$

which describes the Sagnac effect induced by the effective magnetic field in a closed cavity. From Eq. (5), it's clear that the frequency splitting of a pair of CW and CCW modes is proportional to the azimuthal quantum number m and angular velocity Ω. For comparison, a set of representative researches on Sagnac frequency splitting are listed in Table.1 in Appendix A, including inertial frame and co-rotating frame. Surprisingly, Eq. (5) shows good consistency with the formula in second row of Table.1 if the dispersion term is omitted. The explicit expression of rotation-induced effective magnetic field in Eq. (3) and the rigorous relation between the Sagnac frequency splitting and the rotation-induced effective gauge field in Eq. (4) are the first main result of our paper.

3. Results and discussions

3.1. Frequency splitting simulation

We examine the Sagnac frequency splitting of CW and CCW modes using the analytical results of Eq. (4) and the full-wave simulation results obtained from finite-element calculation. Though the rotating disk can be calculated analytically [2,16,17,20], the finite-element model we adopted here can handle generically bianisotropic medium with complex geometric shape [21]. COMSOL Multiphysics with the modified weak form of finite-element formulation [22–25] is used to simulate the rotating disk in this paper. Figure 1(b) shows the real parts of eigenfrequencies of CW and CCW modes with azimuthal number $m = 2$ as a function of dimensionless angular speed $\Omega R/c$, where the solid lines denote the analytical results from Eq. (4) and the symbols denote the simulation results. The analytical results match perfectly well with the simulation results, indicating a linear dependence as $\Omega R/c$. The insets in Fig. 1(b) show the modal profiles of the CW and CCW modes. We note that the mode pair (i.e. CW and CCW modes) are originally degenerated at $\Omega = 0$. As $\Omega R/c$ increases, this degeneracy is lifted, and the profiles of CW and CCW mode carry a 'spinning' chiral feature, as shown by the right insets in Fig. 1(b). It is worthy to point out that the cavity modes examined in this paper is essentially quasi-normal modes with complex eigenfrequencies and finite Q-factors. The finite value of the Q-factor approximately determines the line-shape of cavity resonance, and it turns out to be rather important in determining the modal hybridization and thus the far-field pattern at lower rotation speed, which will be discussed shortly in the next section.

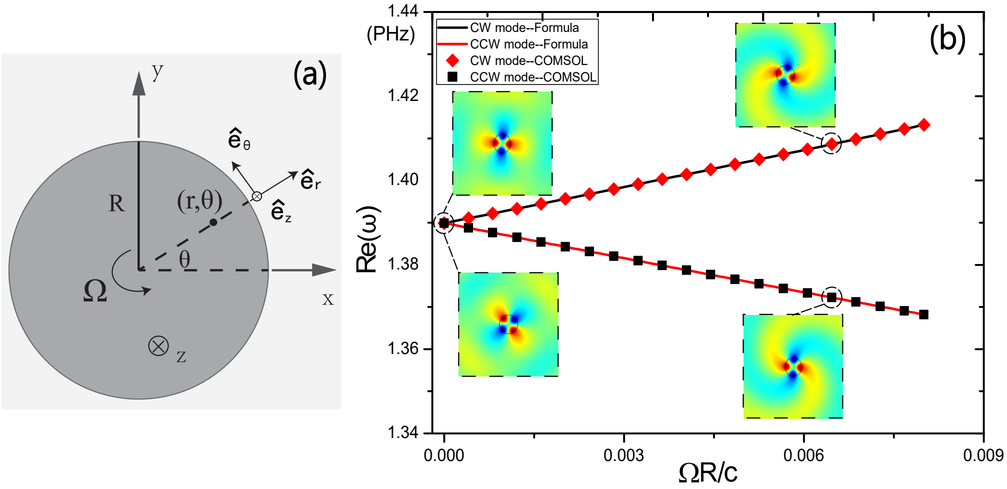

Fig. 1. (a) The structure of a uniformly rotating circular dielectric disk with angular speed Ω. (b) Comparison of results on Sagnac frequency splitting obtained by COMSOL simulation and the analytical expression of Eq. (4). The insets show the E_z components of the modal profiles of CW and CCW mode at $\Omega R/c = 0$ and $\Omega R/c = 0.00646$ obtained by COMSOL simulation. For the simulation, we use vacuum wavelength $\lambda_0 = 1550nm$, disk radius $R = 200nm$ and the relative permittivity $\varepsilon_r = 16$ for the stationary cavity.

3.2. Hybridization of CW and CCW components in a rotating disk

Sagnac frequency shift reflects the modification of the eigenfrequency induced by the rotation. Now we proceed to discuss the impact of rotation upon the eigenfields. It is well understood that the eigenfields for the two split bands due to rotation, as shown in Fig. 1(b), are CW and CCW modes respectively, i.e., $|CW\rangle = E_z(r)\, e^{im\theta}$ and $|CCW\rangle = E_z(r)\, e^{-im\theta}$. In a circular disk, the azimuthal quantum number m is still conserved at a nonzero rotation speed, therefore, CW and CCW modes do not couple with each other. However, a precise one-to-one correspondence between the upper/lower band to the CW/CCW mode only exists at high rotation speed. As discussed in details by Ge [16], a low rotation speed gives rise to a rotation-dependent far-field distribution, indicating a certain mixture of CW and CCW mode.

To reveal the underlying principle behind rotation-dependent far-field distribution, we first identity the modal splitting of $|CW\rangle$ and $|CCW\rangle$ as the rotation speed Ω varies. At $\Omega = 0$, as illustrated in Figs. 2(a) and 2(b), each resonance of the stationary disk has a finite broadening, and the y dimensions represent the normalized resonant amplitude. The full width at half maximum (FWHM), denoted as w in this paper, decreases as the azimuthal quantum number m increases. In the presence of non-zero rotation speed, i.e., $\Omega > 0$, the spectral overlapping between the original eigenmodes $|CW\rangle$ and $|CCW\rangle$ does not vanish, and there is modal splitting $\Delta\omega$ at this situation, as shown in Figs. 2(a) and 2(b). Depending on the relative values between w and $\Delta\omega/2$, the modal splitting can be categorized into two regimes, i.e., weak splitting regime and strong splitting regime, as shown in Figs. 2(a) and 2(b). In strong splitting regime, i.e., $\Delta\omega/2 > w$, the two resonant modes are completely split with negligible spectra overlapping. In contrast, in the weak splitting regime, there is spectral overlapping due to the fact that $\Delta\omega/2 < w$, which gives rise to the rotation-dependent far-field distribution as discussed by Ge [16]. The above analysis gives a qualitative understanding of how $|CW\rangle$ and $|CCW\rangle$ contribute to the eigenfields of the rotating cavity. In the following, we give a quantitatively assessment of how $|CW\rangle$ and $|CCW\rangle$ contribute to the eigenfields of a 2D rotating disk by including the line-shape function explicitly

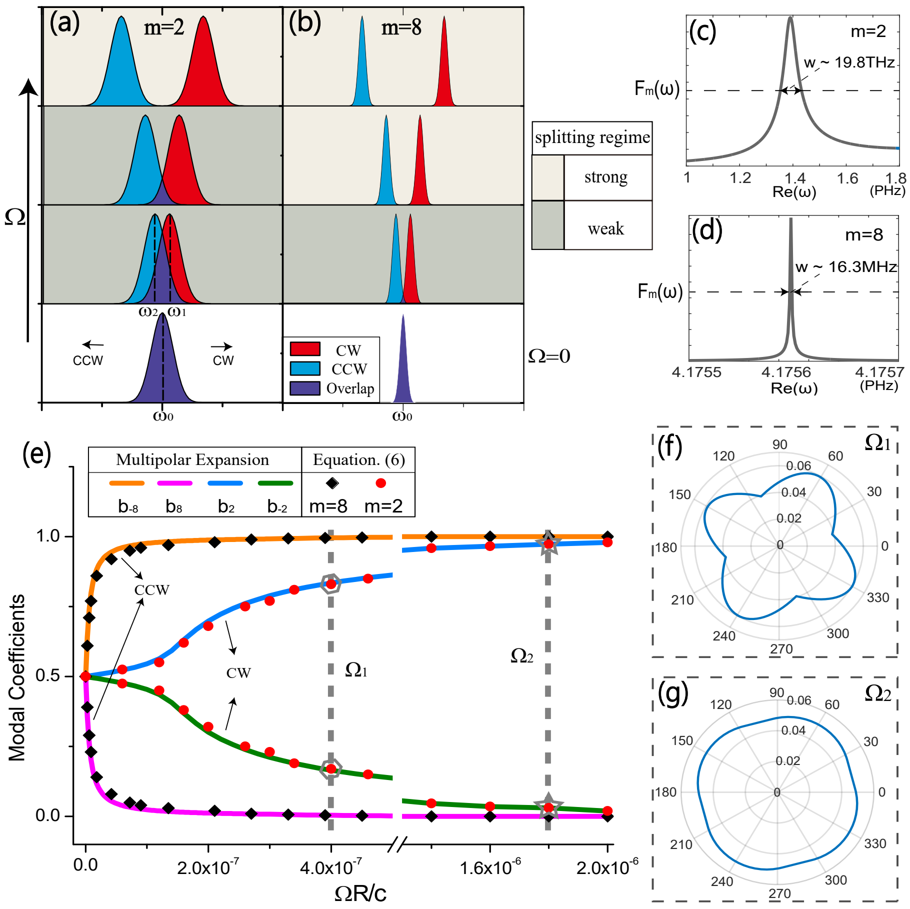

Fig. 2. (a)-(b) Schematic diagrams of the effect of Sagnac frequency splitting on CW/CCW modes for a rotating cavity. Line-shape functions of the modes at $\Omega = 0$ with azimuthal number (c) $m = 2$ and (d) $m = 8$ respectively. (e) The variation of modal coefficients obtained by the multipolar expansion and Eq. (6) for CW mode with azimuthal number $m = 2$ and CCW mode with $m = 8$ versus the dimensionless angular speed $\Omega R/c$. The setup of parameters is shown in Fig. 1. Far-field distribution obtained by superposing the eigenfields $|CW\rangle$ and $|CCW\rangle$ with corresponding ratio at (f) $\Omega_1 R/c = 4 \times 10^{-7}$ and (g) $\Omega_2 R/c = 1.8 \times 10^{-6}$.

in the weak splitting regime.

Due to the circular symmetry, the eigenfield $|\varphi\rangle$ of the stationary disk at Ω=0 can be expressed as $|\varphi\rangle = f_{+m}(\omega, \omega_0)\,|CW\rangle + f_{-m}(\omega, \omega_0)\,|CCW\rangle$, where $f_{+m}(\omega, \omega_0)$ ($f_{-m}(\omega, \omega_0)$) is the line-shape function of CW (CCW) mode with resonant frequency ω_0 and FWHM w (see the definition and detailed calculation of $f_{\pm}(\omega, \omega_0)$ in Appendix B). At $\Omega = 0$, it can be proved that $f_{+m}(\omega, \omega_0)$ is identical to $f_{-m}(\omega, \omega_0)$, i.e., $F_m(\omega, \omega_0) = f_{+m}(\omega, \omega_0) = f_{-m}(\omega, \omega_0)$, so F_m is line-shape function of the stationary cavity mode with azimuthal number m. The precisely calculated line-shape functions of the modes with $m = 2$ and $m = 8$ for the stationary disk are shown in Figs. 2(c) and 2(d), respectively, where the FWHM w is on the order of THz/MHz range. At low rotation speed ($\Delta\omega/2 < w$), to a good approximation, the weighting factors of $f_{\pm}(\omega, \omega_0)$ and the line-shape function $f_{\pm}(\omega, \omega_0)$ remain unchanged, except that the resonant frequencies are shifted by half of the Sagnac frequency splitting. In this regard, the eigenfield of the low-speed rotating disk can be well approximated as follows,

$$|\varphi\rangle = F_m(\omega, \omega_0 + \Delta\omega/2)\,|CW\rangle + F_m(\omega, \omega_0 - \Delta\omega/2)\,|CCW\rangle\,, \tag{6}$$

where $\Delta\omega$ is the Sagnac frequency shift defined in Eq. (4). Evidently, the modal coefficients of the CW/CCW resonance at a certain eigenfrequency ω can be semi-analytically determined by Eq. (6) in the weak splitting regime. This is the second main result of this paper.

In the following, we apply Eq. (6) to quantitatively study the modal hybridization of the rotating disk, accompanied with the numerical verification from multipolar expansion analysis, as shown in Fig. 2(e). Based on the revised finite-element calculation as well as Mie scattering theory [26–28], the multipolar components of the eigenfields can be extracted numerically by projecting the eigenfields of the rotating disk to vector spherical harmonic waves. Surprisingly, the modal coefficients obtained by the full-wave simulation and multipolar expansion agree with the results of our simple analytical model given by Eq. (6), for both the CW mode (orange and magenta for $|m|$=8) and the CCW mode (blue and olive for $|m|$=2), as shown in Fig. 2(e). At Ω=0, it is easy to find that $b_{-m} = b_m$, which is consistent with Eq. (6) at $\Delta\omega$=0. As the disk rotates, the coefficients of the original equal pair of multipolar components for CW (CCW) mode start to differ, with b coefficients increased for m>0 (m<0) and decreased for m<0 (m>0). In comparison, the variation trends of the multipolar components of the CW mode and that of the CCW mode are exactly the opposite. This can be understood by our hybridization model that the Sagnac frequency splitting gives rise to a dominant role of $|CW\rangle(|CCW\rangle)$ in CW (CCW) modes, such that the weighting factor of $|CW\rangle(|CCW\rangle)$ increases (decreases) with angular velocity in CW modes while decreases (increases) in CCW modes. Evidently, b coefficients of the CW mode with $m < 0$ and b coefficients of the CCW mode with $m > 0$ drop to 0 at high rotation speed due to the fact that the Sagnac frequency shift is so large that there is negligible spectra overlapping. We also note that the multipolar components of the cavity mode with large m value are more sensitive to the rotation speed Ω than that of the cavity mode with small m value. This is due to a simple fact that the line-shape function of a higher-order mode has a smaller w, and $\Delta\omega$ with same Ω can easily lead to complete splitting of the higher-order CW and CCW modes.

According to our analysis, the rotation-dependent far-field distribution can be obtained by superposing the eigenfields $|CW\rangle$ and $|CCW\rangle$ with proper weighting factors in accordance with the angular velocity Ω. Taking the CW mode with $m = 2$ in Fig. 2(e) as an example, the far-field distribution at $\Omega_1 R/c = 4 \times 10^{-7}$ and $\Omega_2 R/c = 1.8 \times 10^{-6}$ are shown in Figs. 2(f) and 2(g) respectively. From Fig. 2(f) to Fig. 2(g), the original four-lobed shape gradually becomes a circle, which is consistent with our previous analysis. As long as the angular speed Ω is large enough, the far field has a circular pattern, indicating that only $|CW\rangle$ component exists.

4. Conclusion

In conclusion, we have investigated the optical properties of a rotating cavity beyond the first order approximation. Starting from the first principle of electromagnetism, we have derived the effective magnetic field and Sagnac frequency splitting in a rotating circular dielectric disk from the perspective of synthetic gauge field. With the modified weak form of finite-element model, full-wave simulations are implemented to examine the rotating cavity by treating it as a stationary bianisotropic medium. Moreover, a simple hybridization model is semi-analytically constructed for the disk at a low rotation speed, which provides a simple yet accurate description of the rotation-dependent far-field pattern. Our model is benchmarked against numerical analysis of multipolar expansions and enables a quantitative study of the far-field distribution of the disk at different angular velocity Ω. The results might be applied in the angular speed measurement of rotating devices by monitoring the modification of the far-field distribution. Unlike traditional measurements of angular velocity of rotating systems via Sagnac's interferometer, one only needs to probe the far field with instruments such as CCD cameras, which might have better accuracy without compromise from the distortion of the interferometer or the Doppler frequency shift.

Appendix A: Summary of different formulae of Sagnac frequency shift

Table 1. Various expressions for Sagnac frequency splitting of optical rotating cavities

Formula	Approximation Method	Reference Frame
$\Delta\omega = \frac{2m\Omega}{n^2}$ [1,2,20,29]$\Leftrightarrow\Delta\nu = \frac{2R\Omega}{n\lambda_0}$ [7,30,31]	the wave equation	corotating RF
$\Delta\omega = 2\omega_{rest}\frac{nR\Omega}{c}(1-\frac{1}{n^2}-\frac{\lambda}{n}\frac{dn}{d\lambda})$ [18,32,33]	geometrical optics	inertial RF
$\Delta\nu = \frac{2R\Omega}{\lambda_0}$ [3,34,35]	experiment	inertial RF
$\Delta\nu = \frac{2nR\Omega}{\lambda_0}$ [36]	the wave equation	static medium rotating RF
$\Delta\nu = \frac{\Omega D}{c}\nu_{rest}$ [37,38]	Calibration wave function	inertial RF

Appendix B: Line-shape functions of stationary cavity modes

Starting from the Mie scattering theory, when the incident light is normal to the disk, the coefficient of the scattered field a_m vanishes, and b_m has the following form

$$b_m = \frac{J_m(n\rho_0)J_m'(\rho_0) - nJ_m'(n\rho_0)J_m(\rho_0)}{J_m(n\rho_0)H_m^{(1)'}(\rho_0) - nJ_m'(n\rho_0)H_m^{(1)}(\rho_0)}, \tag{7}$$

where J_m and $H_m^{(1)}$ are Bessel function of first kind and Hankel function, respectively, of integral order m (i.e. angular quantum number). n is the relative refractive index of the disk. $\rho_0 = k_0 R$, $k_0 = \omega/c$ is the wave number in vacuo, ω being the frequency in the time harmonic oscillating field $e^{i\omega t}$, and c is the speed of light in vacuum. R represents the radius of the disk. We define the line-shape function as $f(\omega) = 1/\left(J_m(n\rho_0)H_m^{(1)'}(\rho_0) - nJ_m'(n\rho_0)H_m^{(1)}(\rho_0)\right)$, using the identities $J_m'(x) = \frac{1}{2}\left[J_{m-1}(x) - J_{m+1}(x)\right]$ and $H_m^{(1)'}(x) = \frac{1}{2}\left[H_{m-1}^{(1)}(x) - H_{m+1}^{(1)}(x)\right]$, by varying angular frequency ω, the absolute value of the $f(\omega)$ function of different angular quantum number m are obtained.

As a test, we make a comparison with the results of COMSOL. For example, for the mode with angular quantum number $m = 2$ at $\Omega = 0$, its (angular) eigenfrequency is $1.389925 \times 10^{15} + 1.982725 \times 10^{13}i$, for the other mode with angular quantum number $m = 8$ at rest, its eigenfrequency is $4.175587 \times 10^{15} + 1.627345 \times 10^{7}i$. However, for the CCW mode with azimuthal number $m = 2$ at $\Omega R/c = 1 \times 10^{-6}$, its eigenfrequency becomes $1.389923 \times 10^{15} + 1.982726 \times 10^{13}i$. By approximation, we assume that the imaginary parts of the modes remain unchanged, since the value of $\Omega R/c$ is particularly small($\sim 10^{-6}$) in our considered cases and the real parts of the modes are at least 70 times that of imaginary parts.

Funding

National Natural Science Foundation of China (NSFC) (11874026, 61735006, 61775063); National Key Research and Development Program of China (2017YFA0305200); Fundamental Research Funds for the Central Universities (HUST: 2018KFYYXJJ055, HUST: 2017KFYXJJ027); Research Grants Council of Hong Kong SAR (CityU 21302018).

Acknowledgment

We thank Prof. Wei Liu for fruitful discussions.

References

1. R. Sarma, H. Noh, and H. Cao, "Wavelength-scale microdisks as optical gyroscopes: a finite-difference time-domain simulation study," J. Opt. Soc. Am. B **29**, 1648–1654 (2012).
2. S. Sunada and T. Harayama, "Design of resonant microcavities: application to optical gyroscopes," Opt. Express **15**, 16245–16254 (2007).
3. A. Mignot, G. Feugnet, S. Schwartz, I. Sagnes, A. Garnache, C. Fabre, and J.-P. Pocholle, "Single-frequency external-cavity semiconductor ring-laser gyroscope," Opt. Lett. **34**, 97–99 (2009).
4. L. Ge, R. Sarma, and H. Cao, "Rotation-induced mode coupling in open wavelength-scale microcavities," Phys. Rev. A **90**, 013809 (2014).
5. R. Sarma, L. Ge, J. Wiersig, and H. Cao, "Rotating optical microcavities with broken chiral symmetry," Phys. Rev. Lett. **114**, 053903 (2015).
6. S. Sunada, "Large sagnac frequency splitting in a ring resonator operating at an exceptional point," Phys. Rev. A **96**, 033842 (2017).
7. E. J. Post, "Sagnac Effect," Rev. Mod. Phys. **39**, 475–493 (1967).
8. R. Cook, H. Fearn, and P. Milonni, "Fizeau's experiment and the Aharonov–Bohm effect," Am. J. Phys. **26**, 705–710 (1995).
9. M. Vieira, A. M. d. M. Carvalho, and C. Furtado, "Aharonov-Bohm effect for light in a moving medium," Phys. Rev. A **90**, 012105 (2014).
10. K. Y. Bliokh and Y. P. Bliokh, "Modified geometrical optics of a smoothly inhomogeneous isotropic medium: the anisotropy, Berry phase, and the optical Magnus effect," Phys. Rev. E **70**, 026605 (2004).
11. K. J. Fang, Z. F. Yu, and S. H. Fan, "Photonic Aharonov-Bohm effect based on dynamic modulation," Phys. Rev. Lett. **108**, 153901 (2012).
12. F. Liu and J. Li, "Gauge field optics with anisotropic media," Phys. Rev. Lett. **114**, 103902 (2015).
13. Y. T. Chen, R.-Y. Zhang, Z. F. Xiong, Z. H. Hang, J. Li, J. Q. Shen, and C. T. Chan, "Non-abelian gauge field optics," Nat. Commun. **10**, 3125 (2019).
14. S. B. Wang, G. C. Ma, and C. T. Chan, "Topological transport of sound mediated by spin-redirection geometric phase," Sci. Adv. **4**, eaaq1475 (2018).
15. H. Minkowski, "Die Grundgleichungen für die elektromagnetischen Vorgänge in bewegten Körpern," Nachr. Ges. Wiss. Goettingen, Math.-Phys. Kl. **1**, 53–111 (1908).
16. L. Ge, R. Sarma, and H. Cao, "Rotation-induced evolution of far-field emission patterns of deformed microdisk cavities," Optica **2**, 323–328 (2015).
17. R. Movassagh and S. G. Johnson, "Optical Bernoulli forces," Phys. Rev. A **88**, 023829 (2013).
18. S. Maayani, R. Dahan, Y. Kligerman, E. Moses, A. U. Hassan, H. Jing, F. Nori, D. N. Christodoulides, and T. Carmon, "Flying couplers above spinning resonators generate irreversible refraction," Nature **558**, 569–574 (2018).
19. R. Huang, A. Miranowicz, J.-Q. Liao, F. Nori, and H. Jing, "Nonreciprocal photon blockade," Phys. Rev. Lett. **121**, 153601 (2018).
20. H. Cao and J. Wiersig, "Dielectric microcavities: Model systems for wave chaos and non-Hermitian physics," Rev. Mod. Phys. **87**, 61–111 (2015).
21. J.-W. Dong, X.-D. Chen, H. Y. Zhu, Y. Wang, and X. Zhang, "Valley photonic crystals for control of spin and topology," Nat. Mater. **16**, 298–302 (2017).
22. "COMSOL Multiphysics 5.2: a finite element analysis, solver and simulation software," http://www.comsol.com/.
23. K. Sakoda, *Optical Properties of Photonic Crystals* (Springer Science & Business Media, 2004).
24. W. I. Fushchich and A. G. Nikitin, *Symmetries of Maxwell's Equations* (Springer Science & Business Media, 2013).
25. J. Xu, B. B. Wu, and Y. T. Chen, "Elimination of polarization degeneracy in circularly symmetric bianisotropic waveguides: a decoupled case," Opt. Express **23**, 11566–11575 (2015).
26. C. F. Bohren and D. R. Huffman, *Absorption and Scattering of Light by Small Particles* (John Wiley & Sons, 2008).
27. S. Kozaki, "Scattering of a Gaussian beam by a homogeneous dielectric cylinder," J. Appl. Phys. **53**, 7195–7200 (1982).
28. P. Grahn, A. Shevchenko, and M. Kaivola, "Electromagnetic multipole theory for optical nanomaterials," New J. Phys. **14**, 093033 (2012).
29. J. Scheuer, "Direct rotation-induced intensity modulation in circular Bragg micro-lasers," Opt. Express **15**, 15053–15059 (2007).
30. G. B. Malykin, "Sagnac effect in ring lasers and ring resonators. How does the refractive index of the optical medium influence the sensitivity to rotation?" Physics-Uspekhi **57**, 714–720 (2014).
31. W. Liang, A. Savchenkov, V. Ilchenko, R. Griffith, E. De Cuir, S. Kim, A. Matsko, and L. Maleki, "On Sagnac frequency splitting in a solid-state ring Raman laser," Opt. Lett. **42**, 4736–4739 (2017).
32. G. B. Malykin, "The Sagnac effect: correct and incorrect explanations," Physics-Uspekhi **43**, 1229–1252 (2000).
33. H. Jing, H. Lü, S. Özdemir, T. Carmon, and F. Nori, "Nanoparticle sensing with a spinning resonator," Optica **5**, 1424–1430 (2018).
34. A. H. Rosenthal, "Regenerative circulatory multiple-beam interferometry for the study of light-propagation effects," J. Opt. Soc. Am. **52**, 1143–1148 (1962).
35. R. E. Meyer, S. Ezekiel, D. W. Stowe, and V. J. Tekippe, "Passive fiber-optic ring resonator for rotation sensing," Opt.

Lett. **8**, 644–646 (1983).
36. J. L. Anderson and J. W. Ryon, “Electromagnetic radiation in accelerated systems,” Phys. Rev. **181**, 1765–1774 (1969).
37. C. V. Heer, “Resonant frequencies of an electromagnetic cavity in an accelerated system of reference,” Phys. Rev. **134**, A799–804 (1964).
38. P. K. Cheo and C. V. Heer, “Beat frequency between two traveling waves in a Fabry-Perot square cavity,” Appl. Opt. **3**, 788–789 (1964).